

Realizing valley polarization and valley inversion in graphene by using a valley magnet

Si-Yu Li^{1,§}, Ying Su^{2,§}, Ya-Ning Ren¹, and Lin He^{1,*}

¹ Center for Advanced Quantum Studies, Department of Physics, Beijing Normal University, Beijing, 100875, People's Republic of China

²Theoretical Division, T-4 and CNLS, Los Alamos National Laboratory, Los Alamos, New Mexico 87545, USA

[§]These authors contributed equally to this work.

*Correspondence and requests for materials should be addressed to L.H. (e-mail: helin@bnu.edu.cn).

It is quite easy to control the spin polarization and spin direction of a system via magnetic fields. However, there is no such a direct and efficient way to manipulate the valley pseudospin degree of freedom. Here, we demonstrate experimentally that a valley magnet can switch valley polarization and valley inversion in graphene. The valley magnet is realized by using both strain-induced pseudomagnetic fields and real magnetic fields. The pseudomagnetic fields, which are quite different from real magnetic fields, pointing in opposite directions at the two distinct valleys of graphene. Therefore, the coexistence of the pseudomagnetic fields and the real magnetic fields leads to imbalanced effective magnetic fields at the two distinct valleys of graphene. This allows us to control the valley in graphene as convenient as the electron spin by using the valley magnet. Our results highlight a pathway to valleytronics in strained graphene-based platforms.

Pseudomagnetic field, arising from the modulation of electron hopping due to lattice deformation, can effectively create Landau quantization around the low-energy Dirac cones of graphene¹⁻⁴. Such a pseudo-Landau quantization has been explicitly demonstrated by scanning tunneling microscopy (STM) measurements in which the quantized differential conductance peaks evidently reveal the pseudo-Landau levels⁵⁻⁹. Similar to the real Landau levels (LLs) of graphene under external magnetic field, the energies of pseudo-LLs are proportional to the square root of the pseudomagnetic field strength, exhibiting the unique signature of massless Dirac fermions of graphene. Despite these similarities between the pseudomagnetic field and real magnetic field, there are two fundamental differences between them. First, the pseudomagnetic field, unlike the real magnetic field, does not violate the time-reversal symmetry of graphene. Therefore, it has opposite signs in the K_+ and K_- valleys¹⁻⁴. Second, the pseudomagnetic field direction can be reversed at nanoscale since it is solely determined by the local strain. Such a behavior is almost impossible to be realized for the real magnetic field. These two characteristic features make the pseudomagnetic field a unique method to tune the electronic properties of graphene and many exotic quantum phenomena are predicted in strained graphene¹⁰⁻²¹. Besides these abundant theoretical investigations, solid experimental evidence of the effect of the two characteristic features on the electronic properties of graphene is still largely unexplored. Here, we show that the coupled pseudomagnetic field and real magnetic field can be treated as a valley magnet, which can be used to switch valley polarization and valley inversion in graphene. Our experiment indicates that it is possible to control the valley degree of freedom as

convenient as the electron spin. This is extremely important in the valleytronics based on graphene^{11,12,22-24}.

To study the valley polarization and inversion in strained graphene, we carry out measurements on graphene multilayers grown on Rh foils. By applying strong perpendicular magnetic fields, we can observe well-defined Landau quantization of massless Dirac fermions (Fig. 1), indicating that the topmost graphene sheet is electronically decoupled from the supporting substrate. Previously, we have demonstrated that the mismatch of thermal expansion coefficients between the graphene and the metal substrates can introduce ripples in graphene^{9,25-27}. In our experiment, nanoscale ripples can be easily observed in the topmost graphene sheet, as shown in Fig. 1A (see the supplementary Fig. S1 for more STM image). Therefore, such a system provides an ideal platform to study novel electronic properties induced by the pseudomagnetic fields in graphene monolayer.

In strained graphene, it is quite difficult to generate uniform pseudomagnetic fields¹⁻⁴. Our measurement indicates that the pseudomagnetic fields in the rippled structure depend sensitively on the measured positions, as shown in Fig. 1B and 1C, even when the structure of the ripples only changes slightly, as shown in Fig. 1A (see Fig. S2 for detailed analysis of the strain). Figure 1C shows three representative scanning tunneling spectroscopy (STS) spectra acquired in zero magnetic field on different positions along the ripples. The tunneling peaks in the spectra are attributed to the strain-induced pseudo-LLs, which can be fitted well by the Landau quantization of massless Dirac fermions^{5-9,28-32} (see details in the Supplementary of Fig. S3). According to the fitting,

we can obtain the value of the pseudomagnetic fields. Figure 1B shows distribution of pseudomagnetic fields measured along the arrow in Fig. 1A. Obviously, the pseudomagnetic fields are quite non-uniform and there is a very narrow boundary (less than 2 nm, within two dashed lines in Fig. 1A), where the pseudomagnetic field is almost zero, separating two adjacent regions with nonzero pseudomagnetic fields. The fast Fourier transform (FFT) analysis of the atomic structures (Fig. S2) indicates that the strain in the ripples changes gradually from a compressive strain $\sim 1.5\%$ (above the boundary) to a tensile strain $\sim 1.5\%$ (below the boundary). Our theoretical calculation by taking into account the spatial variation of strain in the rippled structure (Fig. 2A) shows that the direction of pseudomagnetic field is reversed when the strain changes from the tensile strain to compressive strain along ridge of the ripple (Fig. 2B). Thus a narrow boundary with zero pseudomagnetic field exists naturally at the transition point, as shown in Fig. 2B (see supporting materials for details of calculations). The calculated values of the pseudomagnetic fields also agree well with that obtained in our experiment. Therefore, our experimental results, complemented by theoretical calculations, demonstrate that the pseudomagnetic field has opposite signs in the two adjacent regions separating by the narrow boundary in the rippled structure shown in Fig. 1A.

Because of the time-reversal symmetry, the pseudomagnetic field exactly has the same value but has opposite signs in the K_+ and K_- valleys (Fig. 2B). By applying a real magnetic field, the total effective magnetic field in the two valleys becomes different. In graphene monolayer, the energies of $n \neq 0$ LLs depend on the magnetic fields and only the $n = 0$ LL is independent of the magnetic fields. Therefore, we can realize valley

polarization for the $n \neq 0$ LLs by using both the pseudomagnetic fields and real magnetic fields. Figure 1D shows three representative spectra recorded in different positions of the ripple in the presence of a real magnetic field of $B = 11$ T. We can observe well-defined Landau quantization, showing excellent single-layer-graphene scaling with Fermi velocities of $\sim 10^6$ m/s, in the rippled graphene. There is a pronounced asymmetry between the intensities of the LLs with positive orbital index and negative orbital index. This may partly arise from the decrease of quasiparticle lifetimes with the energy difference from the Fermi energy³² and partly arise from large electron-hole asymmetry in strained graphene^{9,26}. Besides the pronounced asymmetry, the other obvious feature of the spectra is the clear splitting of $n = -1$, $n = -2$ and $n = -3$ LLs along with undetectable splitting of the $n = 0$ LL recorded at the positions with finite pseudomagnetic fields, as shown in Fig. 1D (see Fig. S4 for more spectra). At the boundary with zero pseudomagnetic field, the splitting of all the LLs vanishes. These results demonstrate explicitly that the splitting of the LLs is induced by the combined effect of the pseudomagnetic fields and the real magnetic field^{9,13,16}.

The above observations can be reproduced well by taking into account the effects of both strain-induced pseudo-magnetic fields and real magnetic fields on the Landau quantization of massless Dirac fermions in graphene monolayer, as shown in Fig. 2C and Fig. 2D. Our calculation indicates that the coexistence of pseudomagnetic fields and real magnetic fields in the graphene ripple leads to the emergence of valley polarization for the $n \neq 0$ LLs (see supporting materials for details of calculations). In our experiment, the valley splittings of the $n = -2$ and $n = -3$ LLs are not as pronounced

as that of the $n = -1$ LL (Fig. 1D). Such a phenomenon is also well reproduced in our numerical result (Fig. 2C and 2D). Theoretically, the description of modulated electron hopping in strained graphene as an effective pseudo-magnetic field is exactly valid only at the charge neutrality point. Apart from the charge neutrality point, the high pseudo-Landau levels are not well defined and the low-energy effective pseudomagnetic field description fails. Therefore, we can obtain better valley splitting with decreasing LL index for the $n \neq 0$ LLs. Previously, the valley splitting obtained in other materials, such as Si, is usually less than 0.5 meV^{33,34}. In graphene, the valley splitting induced by the coexistence of pseudomagnetic fields and real magnetic fields is easy to reach several tens meV, as shown in Fig. 1D and Fig. 2D.

More importantly, valley inversion can be easily realized in strained graphene when the pseudomagnetic field reverses its directions. Because of the reverse of the pseudomagnetic field around the boundary in the studied ripples, the valley polarization changes signs from positive in the top region to negative in the bottom region, as shown in Fig. 1D, Fig. 2C and Fig. 2D. Here positive (negative) valley polarization is defined as the energy of the LLs in the K_+ valley is larger (smaller) than that in the K_- valley. At the boundary, the valley polarization is zero, which is independent of the real magnetic fields. The above result demonstrates explicitly that the coupled pseudomagnetic field and real magnetic field can be treated as the valley magnet. It is possible to switch valley polarization and valley inversion in graphene by using the valley magnet.

To further measure the spatially varying valley splitting in strained graphene, we use a recently developed method based on edge-free graphene quantum dots (QDs), as

schematically shown in Fig. 3A and 3B. The edge-free graphene QD is generated by combining the electric field of the STM tip with a perpendicular magnetic field^{35,36}. In strained graphene, the coexistence of pseudomagnetic fields and real magnetic fields generated valley-polarized LLs (for the $n \neq 0$ LLs). The probing STM tip, acting as a moveable top gate in the measurement, bends the LLs in the region beneath the tip into the gaps between the LLs, which leads to edge-free confinement in graphene and generates confined orbital states in the QDs (Fig. 3B). Because the confinement is achieved without resorting to physical edges, the orbital states of the edge-free QDs can reflect the degeneracies of electrons in the studied graphene regions, as demonstrated very recently^{35,36}. In pristine graphene, there are four-fold degeneracies (spin and valley) for electronic states. Therefore, every single orbital state of the edge-free QD could be occupied by four electrons (See Fig. S5). Because of the small capacitance C of the edge-free QD, a single excess electron on the graphene QD needs to overcome the electrostatic energy $E_c = e^2/C$. As a consequence, we can observe a series of quadruplets of charging peaks in STS spectrum of pristine graphene (See Fig. S6 for our experimental data on pristine graphene monolayer). When the valley degeneracy is lifted, every single quadruplet of the confined orbital states will be divided into two doublets, as schematically shown in Fig. 3C.

The edge-free QDs is movable with the STM tip, consequently, we can detect the valley splitting E_v of graphene at any position where we chose. Figure 3D shows representative STS spectra recorded on the orange dot in Fig. 1A in different magnetic fields. Besides the well-defined LLs at low bias, we also observed charging peaks at

high bias of the STS spectra, indicating the emergence of the edge-free graphene QD beneath the STM tip. Obviously, the four charging peaks of a bound state divided into two doublets. In our experiment, the first four charging peaks arise from the confinement of the $n = -1$ LL. We define the energy spacing between two nearest peaks of the four peaks as ΔE_{12} , ΔE_{23} and ΔE_{34} , with $\Delta E_{12} = E_c + E_z$, $\Delta E_{23} = E_c + E_v - E_z$, and $\Delta E_{34} = E_c + E_z$ respectively ($E_z = g\mu_B B$ with the effective g -factor $g \approx 2$ is the Zeeman splitting and E_v is valley splitting). Here the energy spacing of the confined states ΔE in the QD can be directly deduced from the voltage difference ΔV_{tip} acquired from the charging peaks in the STS spectra by using $\Delta E = \eta e \Delta V_{tip}$ with η as the tip lever arm^{35,36}. In our experiment, η can be roughly estimated according to the position of -1 LL and the onset of charging peaks in the STS spectra (See Fig. S7 for more analysis). The valley splitting ΔE_v of a selected position can be directly acquired according to $\Delta E_v = \Delta E_{23} - \Delta E_{12} + 2E_z$. In Fig. 3E, we summarize the valley splitting ΔE_v measured in the orange dot of Fig. 1A as a function of real magnetic fields. In the meanwhile, we also plot the valley splitting of the same position deduced from the splitting of the $n = -1$ LL in different magnetic fields in Fig. 3E. Obviously, the valley splitting measured by the two methods agrees well with each other, further demonstrating that it is facile to detect the valley splitting at nanoscale by using the edge-free graphene quantum dot. Figure 3F shows the four charging peaks measured at different positions along the arrow in Fig. 1A. It indicates that the valley splitting depends on the measured positions and reverses the direction around the boundary where the pseudomagnetic field is zero. Such a result is reasonable since that the

pseudomagnetic field reverses the direction along the ripple, as shown in Fig. 1 and Fig. 2.

To clearly show the spatially varying valley splitting, we measured 70×70 spectra in the studied area shown in Fig. 1A at a fixed real magnetic field. Then we can obtain the values of ΔE_{12} (ΔE_{34}), ΔE_{23} and $|\Delta E_v|$ as a function of positions in the studied area. Figures 4A-4C show representative results obtained at $B = 11$ T. Therefore, we obtained the valley splitting in the whole studied area (Fig. 4C). Similar results are obtained in other different real magnetic fields (see Fig. S8). In the narrow boundary with zero pseudomagnetic field, the valley splitting is measured to be zero. Figure 4d summarizes the valley splitting as a function of positions measured along the arrow shown in Fig. 1A in different real magnetic fields. Obviously, there is a narrow boundary with zero valley splitting that separates two adjacent areas with opposite valley splitting. The maximum valley splitting changes from about 20 meV in the top region to -10 meV in the bottom region in the studied area shown in Fig. 1A. Here we should point out that the strain variation from the compressive strain to the tensile strain is critical for the observation of the valley inversion. In strained graphene with only compressive strain (or tensile strain), we still can observe spatially varying valley splitting due to the non-uniform of the pseudomagnetic fields. However, the valley splitting cannot decrease to zero and reverse its direction (see Fig. S9-S11 for more experimental data and analysis).

In summary, our experiments demonstrate that the valley pseudospin can be controlled by the valley magnet. Similar to the Zeeman splitting of electron spins, the valley degeneracy can be lifted by the imbalanced effective magnetic fields at the two

distinct valleys of graphene. The resulted valley-polarized Landau level splitting up to several tens meV provides an ideal two-level subsystem formed purely by valley polarized quantum states. Because the tensile strain and compressive strain generate opposite pseudomagnetic fields, the valley polarization can be tuned at nanoscale by the strain engineering of graphene sheets. Our results provide a new avenue to manipulate valley pseudospin degree of freedom by the valley magnet, which may have potential applications in graphene-based valleytronics.

Acknowledgments

This work was supported by the National Natural Science Foundation of China (Grant Nos. 11674029, 11422430, 11374035), the National Basic Research Program of China (Grants Nos. 2014CB920903, 2013CBA01603). L.H. also acknowledges support from the National Program for Support of Top-notch Young Professionals and support from “the Fundamental Research Funds for the Central Universities”. Y.S. was supported by the U.S. Department of Energy through the Los Alamos National Laboratory LDRD program.

References:

1. Vozmediano, M. A. H., Katsnelson, M. I., Guinea, F. Gauge fields in graphene. *Phys. Rep.* **496**, 109-148 (2010).
2. Guinea, F., Katsnelson, M. I., Geim, A. K. Energy gaps and a zero-field quantum Hall effect in graphene by strain engineering. *Nature Phys.* **6**, 30-33 (2010).
3. Guinea, F., Katsnelson, M. I., Vozmediano, M. A. H. Midgap states and charge inhomogeneities in corrugated graphene. *Phys. Rev. B* **77**, 075422 (2008).
4. Guinea, F., Horovitz, B., Le Doussal, P. Gauge field induced by ripples in graphene. *Phys. Rev. B* **77**, 205421 (2008).

5. Levy, N., Burke, S. A., Meaker, K. L., Panlasigui, M., Zettl, A., Guinea, F., Castro Neto, A. H., Crommie, M. F. Strain-induced pseudo-magnetic fields greater than 300 Tesla in graphene nanobubbles. *Science* **329**, 544 (2010).
6. Yan, W., He, W.-Y., Chu, Z.-D., Liu, M., Meng, L., Dou, R.-F., Zhang, Y., Liu, Z., Nie, J.-C., He, L. Strain and curvature induced evolution of electronic band structures in twisted graphene bilayer. *Nature Commun.* **4**, 2159 (2013).
7. Meng, L., He, W.-Y., Zheng, H., Liu, M., Yan, H., Yan, W., Chu, Z.-D., Bai, K. K., Dou, R.-F., Zhang, Y., Liu, Z., Nie, J.-C., He, L. Strain-induced one-dimensional Landau level quantization in corrugated graphene. *Phys. Rev. B* **87**, 205405 (2013).
8. Yan, H., Sun, Y., He, L., Nie, J.-C., Chan, M. H. W. Observation of Landau-level-like quantization at 77 K along a strained-induced graphene ridge. *Phys. Rev. B* **85**, 035422 (2012).
9. Li, S.-Y., Bai, K.-K., Yin, L.-J., Qiao, J.-B., Wang, W.-X., He, L. Observation of unconventional splitting of Landau levels in strained graphene. *Phys. Rev. B* **92**, 245302 (2015).
10. de Juan, F., Cortigo, A., Vozmediano, M. A. H., Cano, A. Aharonov-Bohm interferences from local deformations in graphene. *Nature Phys.* **7**, 810-815 (2011).
11. Wu, Z., Zhai, F., Peeters, F. M., Xu, H. Q., Chang, K. Valley-dependent Brewster angles and Goos-Hanchen Effect in strained graphene. *Phys. Rev. Lett.* **106**, 176802 (2011).
12. Low, T., Guinea, F. Strain-induced pseudomagnetic field for novel graphene electronics. *Nano Lett.* **10**, 3551 (2010).
13. Roy, B. Odd integer quantum Hall effect in graphene. *Phys. Rev. B* **84**, 035458 (2011).
14. Abanin, D. A., Pesin, D. A. Interaction-induced topological insulator states in strained graphene. *Phys. Rev. Lett.* **109**, 066802 (2012).
15. Uchoa, B., Barlas, Y. Superconducting states in Pseudo-Landau-levels of strained graphene. *Phys. Rev. Lett.* **111**, 046604 (2013).
16. Roy, B., Hu, Z.-X., Yang, K. Theory of unconventional quantum Hall effect in strained graphene. *Phys. Rev. B* **87**, 121408(R) (2013).
17. Zhang, D.-B., Seifert, G., Chang, K. Strain-induced pseudomagnetic fields in twisted graphene nanoribbons. *Phys. Rev. Lett.* **112**, 096805 (2014).
18. Wakker, G. M. M., Tiwari, R. P., Blaauboer, M. Localization and circulating currents in curved graphene devices. *Phys. Rev. B* **84**, 195427 (2011).

19. Amorim, B., Cortijo, A., de Juan, F., Grushin, A. G., Guinea, F., Gutierrez-Rubio, A., Ochoa, H., Parente, V., Roldan, R., San-Jose, P., Schiefele, J., Sturla, M., Vozmediano, M. A. H. Novel effects of strains in graphene and other two dimensional materials. *Phys. Rep.* **617**, 1 (2016).
20. Settnes, M., Power, S. R., Jauho, A.-P. Pseudomagnetic fields and triaxial strain in graphene. *Phys. Rev. B* **93**, 035456 (2016).
21. Settnes, M., Power, S. R., Brandbyge, M., Jauho, A.-P. Graphene nanobubbles as valley filters and beam splitters. *Phys. Rev. Lett.* **117**, 276801 (2016).
22. Gorbachev, R. V., Song, J. C. W., Yu, G. L., Kretinin, A. V., Withers, F., Cao, Y., Mishchenko, A., Grigorieva, I. V., Novoselov, K. S., Levitov, L. S., Geim, A. K. Detecting topological currents in graphene superlattices. *Science* **346**, 448 (2014).
23. Wallbank, J. R., Ghazaryan, D., Misra, A., Cao, Y., Tu, J. S., Piot, B. A., Potemski, M., Pezzini, S., Wiedmann, S., Zeitler, U., Lane, T. L. M., Morozov, S. V., Greenaway, M. T., Eaves, L., Geim, A. K., Fal'ko, V. I., Novoselov, K. S., Mishchenko, A. Tuning the valley and chiral quantum state of Dirac electrons in van der Waals heterostructures. *Science* **353**, 575 (2016).
24. Li, J., Zhang, R.-X., Yin, Z., Zhang, J., Watanabe, K., Taniguchi, T., Liu, C., Zhu, J. A valley valve and electron beam splitter. *Science* **362**, 1149 (2018).
25. Bai, K.-K., Zhou, Y., Zheng, H., Meng, L., Peng, H., Liu, Z., Nie, J.-C., He, L. Creating one-dimensional nanoscale periodic ripples in a continuous mosaic graphene monolayer. *Phys. Rev. Lett.* **113**, 086102 (2014).
26. Bai, K.-K., Wei, Y.-C., Qiao, J.-B., Li, S.-Y., Yin, L.-J., Yan, W., Nie, J.-C., He, L. Detecting giant electron-hole asymmetry in a graphene monolayer generated by strain and charged-defect scattering via Landau level spectroscopy. *Phys. Rev. B* **92**, 121405(R) (2015).
27. Meng, L., Su, Y., Geng, D., Yu, G., Liu, Y., Dou, R.-F., Nie, J.-C., He, L. Hierarchy of graphene wrinkles induced by thermal strain engineering. *Appl. Phys. Lett.* **103**, 251610 (2013).
28. Zhang, Y. *et al.* Scanning tunneling microscopy of the π magnetism of a single carbon vacancy in graphene. *Phys. Rev. Lett.* **117**, 166801 (2016).
29. Luican, A., Li, G., Reina, A., Kong, J., Nair, R. R., Novoselov, K. S., Geim, A. K., Andrei, E. Y. Single-Layer Behavior and Its Breakdown in Twisted Graphene Layers. *Phys. Rev. Lett.* **106**, 126802 (2011).

30. Yin, L.-J., Li, S.-Y., Qiao, J.-B., Nie, J.-C., He, L. Landau quantization in graphene monolayer, Bernal bilayer, and Bernal trilayer on graphite surface. *Phys. Rev. B* **91**, 115405 (2015).
31. Miller, D. L., Kubista, K. D., Rutter, G. M., Ruan, M., de Heer, W. A., First, P. N., Strosio, J. A. Observing the quantization of zero mass carriers in graphene. *Science* **324**, 924 (2009).
32. Song, Y. J., et al. High-resolution tunneling spectroscopy of a graphene quartet. *Nature* **467**, 185 (2010).
33. Yang, C. H. et al Spin-valley lifetimes in a silicon quantum dot with tunable valley splitting. *Nat. Commun.* **4**, 2069 (2013).
34. Mi, X., Peterfalvi, C. G., Burkard, G., Petta, J. High-resolution valley spectroscopy of Si quantum dots. *Phys. Rev. Lett.* **119**, 176803 (2017).
35. Freitag, N. M., Chizhova, L. A., Nemes-Incze, P., Woods, C. R., Gorbachev, R. V., Cao, Y., Geim, A. K., Novoselov, K. S., Burgdorfer, J., Libisch, F., Morgenstern, M. Electrostatically confined monolayer graphene quantum dots with orbital and valley splittings. *Nano Lett.* **16**, 5798 (2016).
36. Freitag, N. M., Reisch, T., Chizhova, L. A., Nemes-Incze, P., Holl, C., Woods, C. R., Gorbachev, R. V., Cao, Y., Geim, A. K., Novoselov, K. S., Burgdorfer, J., Libisch, F., Morgenstern, M. Large tunable valley splitting in edge-free graphene quantum dots on boron nitride. *Nature Nano.* **13**, 392-397 (2018).

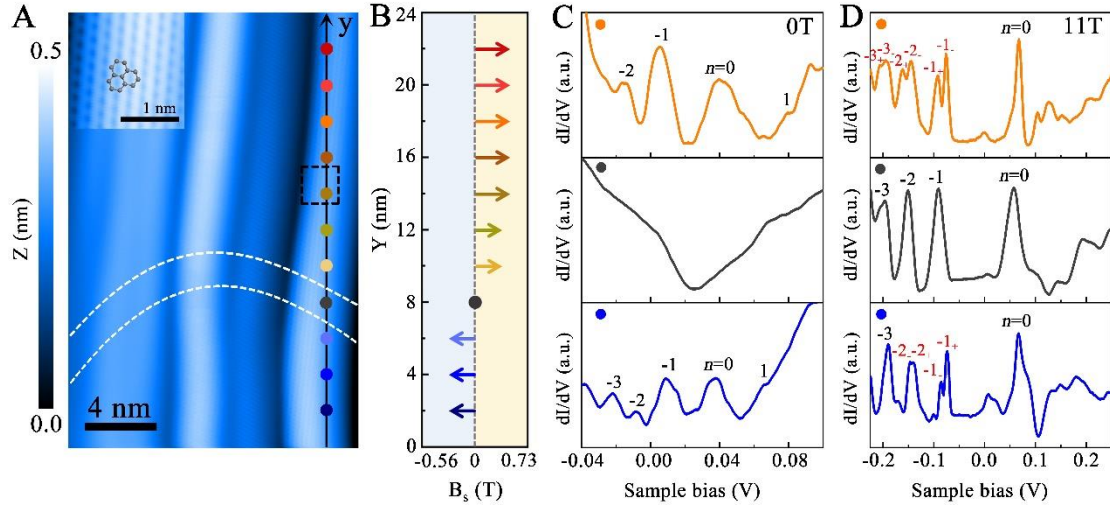


Figure 1. Pseudomagnetic fields and valley-polarized LLs in graphene ripples. A. A $16 \text{ nm} \times 24 \text{ nm}$ STM image ($V_{\text{sample}} = 400 \text{ mV}$ and $I = 0.3 \text{ nA}$) of strained graphene with nanoscale ripples. The black arrow and the dots in different colors mark the positions where we take the STS spectra. The inset shows atomic image of graphene in the black frame. In the region between the two dashed curves, the measured pseudomagnetic field is zero and we cannot detect valley-polarized LLs. **B.** Measured pseudomagnetic fields along the arrow in panel A. **C.** Three tunnelling spectra measured at different positions in panel A in zero real magnetic field. The indexes for the pseudo-Landau levels are marked. **D.** Three tunnelling spectra measured at different positions in panel A in real magnetic field $B = 11 \text{ T}$. The indexes for the LLs are marked. The subscript \pm represents LLs of the K_+/K_- valley.

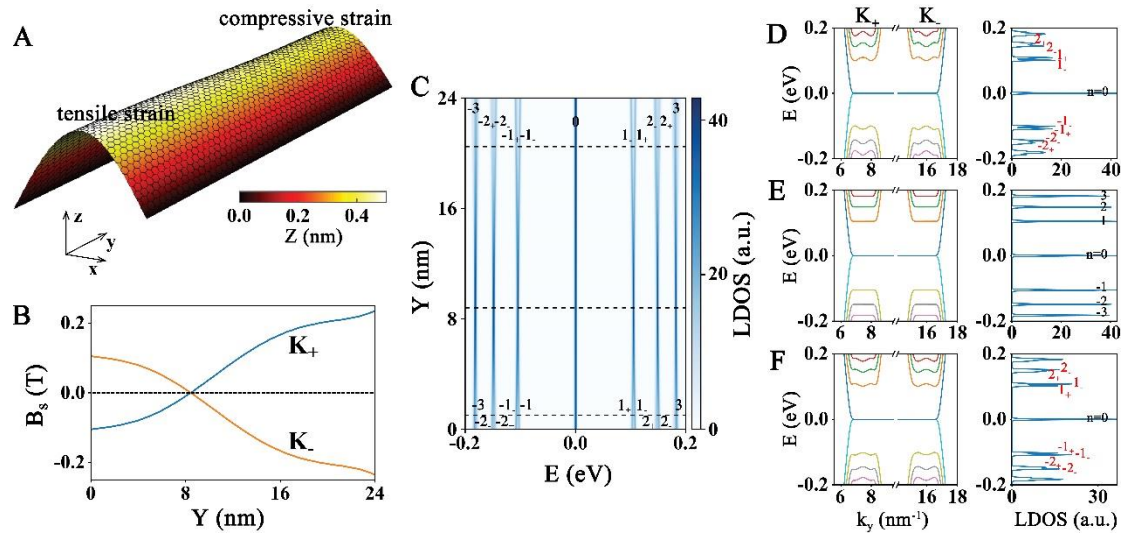


Figure 2. Calculated pseudomagnetic fields and Landau quantization along the graphene ripple. **A.** Sketch of the graphene ripple whose height is from the STM data shown in Fig. 1A. There is a compressive strain in the upper region and a tensile strain in the lower region of the ripple. **B.** Pseudomagnetic fields along the ridge of the ripple at the K_+ and K_- valleys, which are opposite to each other. Pseudomagnetic fields are reversed to opposite direction at the crossing point. **C.** Local density-of-states (LDOS) along the ridge of the ripple at real magnetic field $B = 11$ T. Here the $0, \pm 1, \pm 2, \pm 3$ LLs are included. Splittings of the ± 1 and ± 2 LLs are clearly shown around the two ends of the ripple where the graphene undergoes tensile and compressive strains, respectively. **D, E, F.** Electronic structures (left panels) and the corresponding LDOS (right panels) at different positions of the graphene ripple, corresponding to the three dashed lines (from up to down) in **C**.

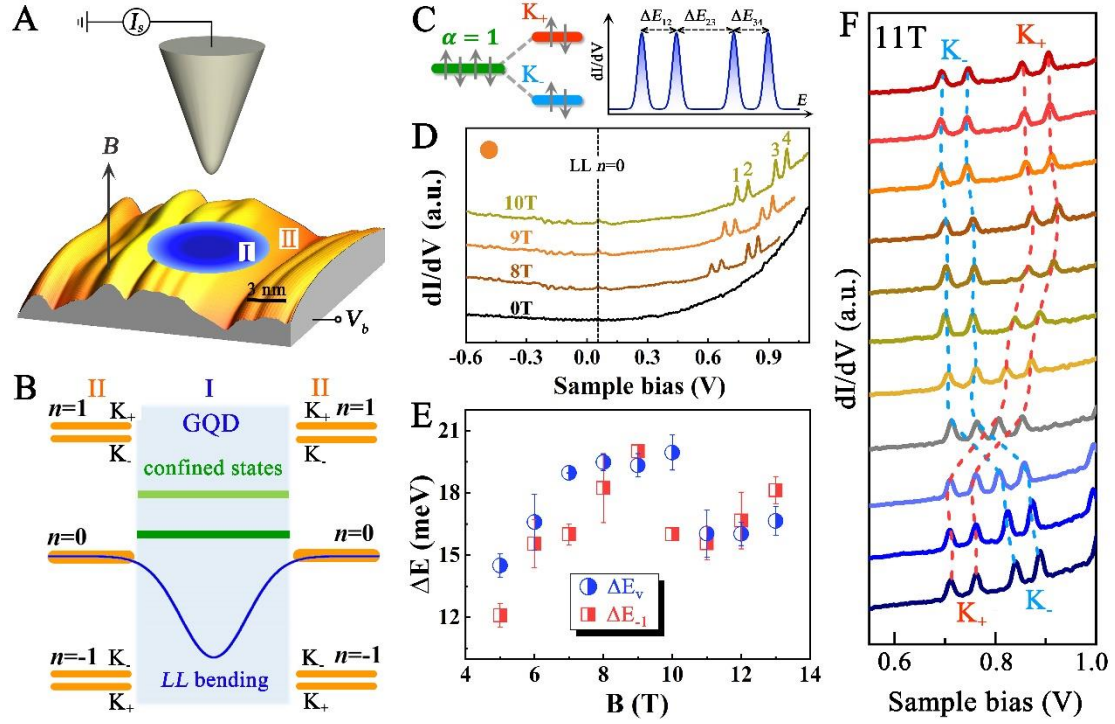


Figure 3. Detecting valley splitting at nanoscale in the strained graphene. **A.** Sketch of the STM experiment on the strained graphene with nanoscale ripples in the presence of magnetic fields. The strained graphene is divided into two regions: one is the graphene region beneath the STM tip (region I), the other is the surrounding graphene region (region II). **B.** Schematic image of the tip-induced edge-free GQDs on strained graphene with the valley-polarized ± 1 LLs. **C.** Left panel: Schematic confined state in the edge-free GQD on strained graphene, exhibiting the valley splitting. Right panel: Schematic for a sequence of doublet charging peaks in the dI/dV spectra detecting in the strained graphene. **D.** The STS spectra taken from the position marked by the orange dot in Fig. 1A in different magnetic fields. The numbers 1-4 sign the sequence of doublet charging peaks. The position of LL_0 is also marked. **E.** Summarizing the values of valley splitting in different magnetic fields, yielding from the sequence of charging peaks (ΔE_v) and the splitting of the LL_{-1} (ΔE_{-1}), respectively. **F.** 11 STS spectra taken along the arrow of Fig. 1A in a real magnetic field of 11 T. We clearly observe a spatially varying valley polarization and valley inversion in the spectra.

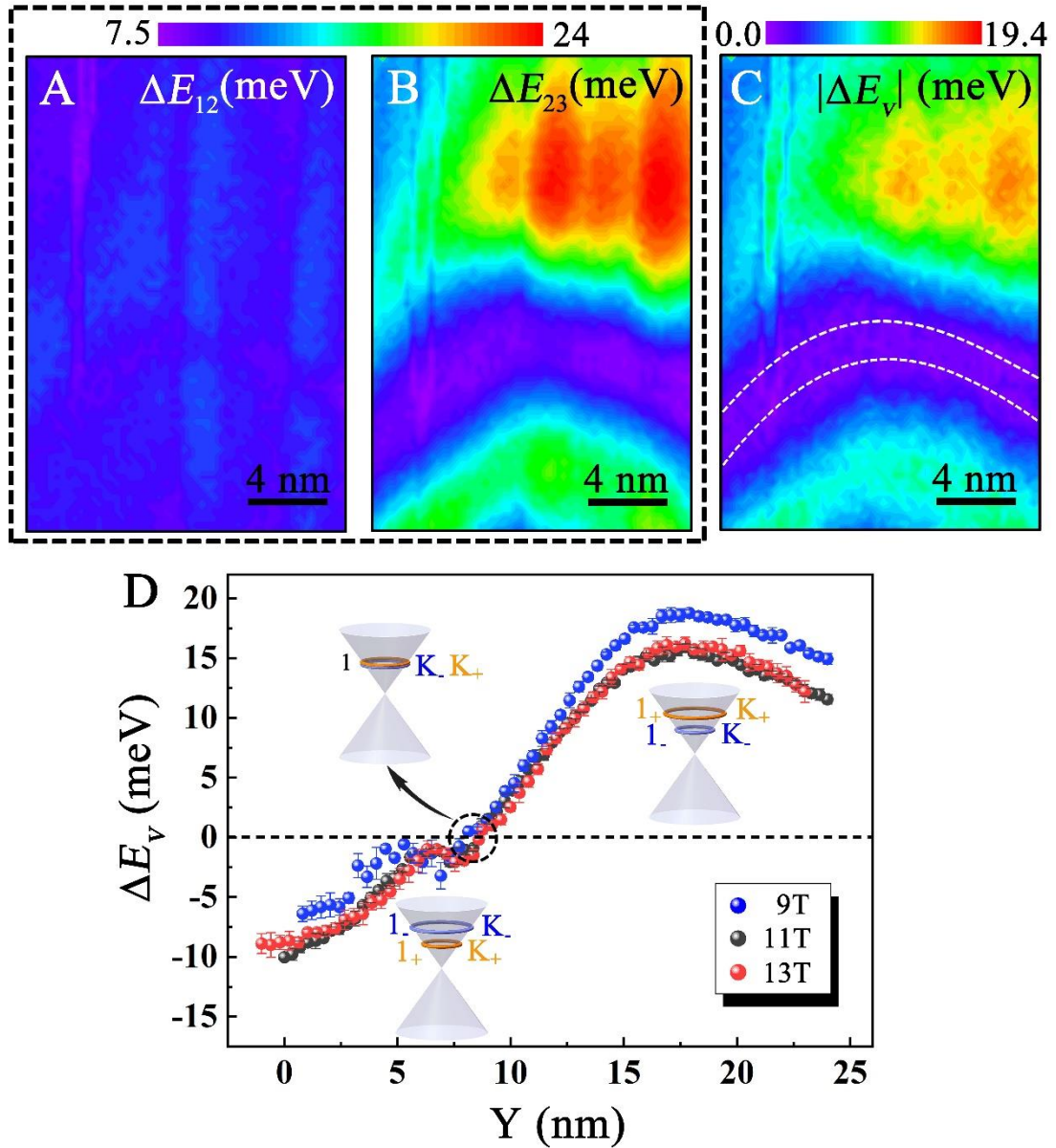


Figure 4. Spatially varying valley splitting and valley inversion in the strained graphene. A-C. $16 \text{ nm} \times 24 \text{ nm}$ energy maps for the values of ΔE_{12} , ΔE_{23} and $|\Delta E_v|$ as a function of positions in the studied area shown in Fig. 1A in 11 T. D. The valley splitting as a function of positions measured along the arrow shown in Fig. 1A in different magnetic fields. The insets schematically show the valley splitting and valley inversion.